City Research Online

City St George's, University of London

Citation: Kantartzis, P., Abdi, M. & Liatsis, P. (2013). Stimulation and measurement patterns versus prior information for fast 3D EIT: A breast screening case study. Signal Processing, 93(10), pp. 2838-2850. doi: 10.1016/j.sigpro.2012.06.027

This is the accepted version of the paper.

This version of the publication may differ from the final published version. To cite this item please consult the publisher's version.

Permanent repository link: https://openaccess.city.ac.uk/id/eprint/7741/

Link to published version: https://doi.org/10.1016/j.sigpro.2012.06.027

Copyright and Reuse: Copyright and Moral Rights remain with the author(s) and/or copyright holders. Copies of full items can be used for personal research or study, educational, or not-for-profit purposes without prior permission or charge, unless otherwise indicated, provided that the authors, title and full bibliographic details are credited, a hyperlink and/or URL is given for the original metadata page and the content is not changed in any way. For full details of reuse please refer to City Research Online policy.

City Research Online: http://openaccess.city.ac.uk/ publications@citystgeorges.ac.uk

*Manuscript
Click here to view linked References

Stimulation and measurement patterns versus prior information for fast 3D EIT: A breast screening case study

Panagiotis Kantartzis[a,*], Montaserbellah Abdi[a], Panos Liatsis[a]

[a] *Information Engineering and Medical Imaging Group, EEIE, SEMS, City University London, Northampton Square, EC1V 0HB, London, UK*

Abstract

Imposing prior information is a typical strategy in inverse problems in return for a stable numerical algorithm. For a given imaging system configuration, the Picard stability condition could then be deployed as a practical measure of the performance of the system against noise contaminated data. Herein, we make extensive use of the above measure to quantify the performance of impedance imaging systems for various stimulation protocols. We numerically demonstrate that a large number of electrodes, as required for breast imaging, adds little value, if any, to the performance of the impedance imaging system. On the other hand, by engaging more electrodes to the 3D firing process, a step increase in performance is recorded. Numerical results on a female breast phantom reveal that for a conventional combination of stimulation and prior information, the potential of the imaging system is approximately 15%. In contrast, for the proposed stimulation and a better prior,

*Corresponding author at: Information Engineering and Medical Imaging Group, EEIE, SEMS, City University London, Northampton Square, EC1V 0HB, London, UK, Tel: +44 (0) 207040 3886, FAX: +44 (0) 207040 8568

Email address: p.kantartzis@city.ac.uk (Panagiotis Kantartzis)

recorded performance is 61% and 97%, respectively. Finally, since a smaller number of electrodes participate in the measurement process, a significantly reduced number of observable data is acquired. It is worth underlining, that despite the reduction in measurements no compromise in the quality of the reconstructed image is reported.

Keywords: Electrical Impedance Tomography, stimulation protocol, measurement protocol, SVD, Picard's criterion, breast screening

1. Introduction

Despite the advances in medicine and diagnostic technology, cancer is still one of the top causes of death, if not the leading one on the global scale. WHO, the World Health Organisation, on its February 2012 fact sheet, reports that *'deaths from cancer worldwide are projected to continue to rise to over 13.1 million in 2030'* [1]. In particular, lung, stomach, liver, colon and breast cancer cause the most cancer deaths each year.

In the UK alone, *'breast cancer is the second biggest cause of death from cancer for women, after lung cancer. On average, nearly 50,000 people are diagnosed with breast cancer each year. That is one person every 10 minutes'* [2]. As breast cancer is one of the most common cancer types and has higher cure rates if detected early [1], there is an all-time-high interest in the development of fast & robust screening modalities for breast cancer.

The gold standard for breast screening is essentially Mammography, often coupled with Magnetic Resonance Imaging (MRI). However, both Mammography and MRI suffer from low specificity rates [3, 4]. In fact, a relatively high rate of raising false positive screenings is frequently encountered, entailing

additional costs for the healthcare system but, more importantly, additional distress for the patient. One should also factor in that patients subject to Mammography screening are exposed to ionizing radiation.

On the other hand, in breast MRI, a contrast agent need to be used [5], also known to produce toxic side effects for the patients. In addition, in younger ages where the breast tissue is denser, Mammography fails to pick abnormalities so Ultrasound appears to be more appropriate [6]. Therefore, as specificity of current imaging modalities is not adequate, further development of alternative techniques is highly desirable. Herein, we omit to discuss methods not fully-approved by the US Food and Drug Administration as screening tools for breast cancer, e.g., Thermography, CT Laser Mammography.

Electrical Impedance Tomography (EIT) is also being investigated in the field of breast imaging as a complementary technique to Mammography for breast cancer detection. Unlike MRI, EIT is portable, inexpensive and in a similar spirit to Ultrasound it does not use ionizing radiation. It is also worth underlining that EIT is already successful in providing valuable insight in both industrial and medical applications [7]. Moreover, commercial versions of EIT systems are now available in routine clinical use [8]. As the electrical properties of normal and malignant breast tissue differ [9], an early commercial development for breast screening, T-scan, has been developed [10]. T-scan has received approval by the US Food and Drug Administration to be used as a diagnostic aid to Mammography as it has been demonstrated to improve sensitivity and specificity. Hence, there is an all-time-high interest in further pursuing research to establish whether EIT could further improve

reported specificity rates, if not survive as a stand alone screening modality in this field.

In principle, EIT is simple and easy to operate and requires no experienced clinicians to perform a scan. In a typical experiment, currents are applied through electrodes attached to the periphery of a body and voltage measurements are collected from some other surface electrodes. The observed data vector, i.e., voltage measurements, is then fed to a computer to estimate the interior material (tissue) distribution [11–15].

Not many will argue that most of the numerical effort is typically allocated to the image reconstruction aspects of the EIT problem. Unlike standard imaging methods, as for instance xray-CT, in EIT one could model, study and demonstrate how a 'local' perturbation affects not only nearby measurements but, crucially, all measurements [11]. Despite the fact that captured measures are sensitive to local perturbations, little is reported on how to optimise driving patterns that produce more valuable measurements and thus reconstructions. Recall that measurements is the only observable data vector.

It is worth mentioning the reports [16, 17], where the authors derived patterns that maximise the distinguishability between two corresponding materials or simply the anticipated reconstruction contrast. Briefly, the idea is to maximise the difference between the two Neuman-to-Dirichlet (NtD) maps. In a circular domain, the optimal stimulation pattern accounts for the eigenvalues of the corresponding NtD functional, i.e., firing on electrodes with Fourier bases. Although this provides an excellent solution from a mathematical point of view, there are some practical limitations of the suggested

method. For instance, one needs to drive a pattern on all electrodes and then measure the resulting voltages on same (current carrying) electrodes. Hence, more practical patterns are sought.

In a 3D setting, there is a greater flexibility in stimulating the object. The authors in [18], suggested some measures to assess available stimulation protocols. Amongst many, their findings encouraged non-adjacent electrode patterns. Further, since for a given set of driving patterns, measurements are subject to a reconstruction (and thus regularisation) algorithm, results could be significantly enhanced or deteriorated. It is not clear therefore, how to best stimulate an object in order to get the most out of a measurement data set. This simply means, that the way that the object is stimulated could either enhance or obscure information content. See [19] for a discussion on information content for EIT.

In the context of breast imaging, the reconstruction situation could be much less trivial mainly due to practical limitations. For instance, a large array of electrodes needs to be attached to the easily deformable female breast. Since both the number of electrodes and hence measurements as well as model misfits of the actual boundary surface are said to affect the quality of the reconstructed image [20], one encounters a potential bottleneck on how to proceed. The latter can be addressed by optical measurements that could result is accurate representations of the female breast surface [21]. However, there is no straightforward way as to which stimulation pattern would provide best results for the breast domain at hand and, of course, under what constraints.

To alleviate this, the authors in [22] proposed plane-wise sinusoidal volt-

age patterns with different phases per plane, that provide improved images. Assuming that a phase difference is the way forward for breast EIT screening, the question on whether one takes the most out of the available EIT system, as some of the measurements are (numerically) linearly dependent, is still open. In sort, this implies that one would eventually need to compensate for this loss by means of penalising higher frequency solutions, i.e., regularisation, to avoid numerical instability. Needless to say that determining the optimal number of electrodes is also an additional open issue.

In the same spirit, the authors in [23] identified the stimulation shortcomings and proposed a much promising strategy which was numerically demonstrated in a 2D setting with 32 electrodes. Unlike most conventional methods reported in literature, the novelty lies in engaging 4 electrodes to act as group and then use 2 such groups of 4 electrodes to drive a current pattern. The authors, by means of Generalised Singular Value Decomposition (GSVD), derived a measure to quantify collected measurements against prior information as well as measurement noise, in order to filter out problematic singular values.

In this paper, we follow the guidelines of [23], as, in our view, this appears to be the only practical measure that factors in prior information when devising a stimulation strategy. Further, we extend the stimulation protocol to 3D, where a greater number of electrodes and patterns is often available. To the best of our knowledge, this methodology has never been tested to a 3D domain before. On the other hand, our contribution differs from the one in [23] as we account for groups of variable electrode numbers to apply the desired stimulation protocol. This implies a variable reduction in the num-

ber of collected measurements (and thus data acquisition timings) without compromising on the quality of the reconstructed images. Finally, there is no need to measure on current carrying electrodes, e.g., [16, 22].

In the next section, a brief introduction to the theoretical framework of EIT is given. The Singular Value Decomposition (SVD) along with the GSVD are also provided as a means of studying a reconstruction stability criterion (Picard's criterion) in Section 3. Next, the suggested 3D stimulation scheme is demonstrated in Section 4 on a simple cylindrical tank and performance is reported against conventional stimulation patterns. The methodology is then carried over to Section 5 which is concerned with a female breast phantom, where further numerical results are presented. Discussion and conclusions finalise this article.

2. Theory: EIT problem

The goal in EIT is to successfully derive a stable numerical map between observable voltages and unobservable interior admittivity distribution(s) in order to infer desirable material/tissue information.

There are two computational models in literature for the EIT; a higher frequency one [24] and a lower frequency one [25]. The latter is freely available from the EIDORS repository [26] whilst, nowadays, represent a widely accepted and used testbench. Therefore, without loss of generality, we omit the high-frequency model and we focus on the low-frequency one.

2.1. The forward problem

According to the EIT-adapted adjoint fields method [27], the process of simulating the boundary surface electrode voltages (i.e., assembling the so

called forward operator in EIT) requires repeated solutions of a generalised Laplacian PDE of non-constant coefficient, subject to appropriate boundary conditions [28] of the form

$$\begin{aligned} \nabla \cdot (\sigma \nabla u) &= 0 \qquad \text{in } \Omega \\ \sigma \nabla u \cdot \nu &= \imath \qquad \text{on } \Gamma \\ u + z_\ell \sigma \nabla u \cdot \nu - U_\ell &= 0 \qquad \text{on } \Gamma_\ell \end{aligned} \tag{1}$$

where $\sigma, u, U_\ell, \nu, \imath, z_\ell$ are the admittivity, the interior potential distribution, the surface potential on the $\ell-$th electrode, the outward unit normal vector, the current density and the surface impedance, respectively. Additional boundary conditions on the interelectrode gaps Υ require that

$$\sigma \nabla u \cdot \nu = 0 \quad \text{on } \Upsilon. \tag{2}$$

$\Omega \subset \Re^3$ is a bounded domain equipped with L electrodes attached on its Lipschitz boundary surface $\partial\Omega$. $\Gamma \subset \partial\Omega$ is the union of areas under each electrode, assumed to be open connected subsets $\bigcup_{\ell=1}^{L} \Gamma_\ell = \Gamma$, whose closures are disjoint, $\bigcap_{\ell=1}^{L} \overline{\Gamma}_\ell = \emptyset$. $\Upsilon := \partial\Omega \setminus \Gamma$ is the union of the remaining areas. Defining the sesquilinear form as [28]

$$a_\Omega((v,V),(w,W)) := \int_\Omega \sigma \nabla v \cdot \nabla \overline{w}\, d\Omega + \sum_{\ell=1}^{L} \int_{\Gamma_\ell} \frac{1}{z_\ell} (v - V_\ell)(\overline{w} - \overline{W}_\ell)\, ds_{\Gamma_\ell}, \tag{3}$$

the weak formulation of the EIT problem on the original domain Ω can be stated as the following direct Boundary Value Problem (BVP): Given a (c-th) driving pattern (currents) $I^{(c)} := (I_1, \ldots, I_L)^T \in \mathbb{R}^L$ find $(u, U) \in \mathcal{H}^1_\Omega$ such that

$$a((u,U),(v,V)) = \sum_{\ell=1}^{L} I_\ell \overline{V}_\ell \qquad \text{for all } (v,V) \in \mathcal{H}^1_\Omega \tag{4}$$

where I_ℓ denotes the current applied to the ℓ-th electrode and $\mathcal{H}^1_\Omega := \{\mathcal{H}^1(\Omega) \oplus \Im^L\}/\Im$ is the (quotient) solution space. Equation (4) requires repeated solutions for the various driving patterns $I^{[d]} := (I^{(1)}, I^{(2)}, \ldots, I^{(d)}) \in \mathbb{R}^{L\times d}$ that form the stimulation pattern $I^{[d]}$. In addition, solutions of m-adjoint stimulation patterns $I^{[m]} \in \mathbb{R}^{L\times m}$ are also required [27]. Intuitively, varying the number of stimulation patterns directly affects the number of required solutions for the PDE, Equation (4). Given that EIT is typically concerned with large-scale Finite Element systems, 'short' patterns ($d \ll$) are favoured as they offer significant computational savings. Hence, it is not hard to infer that the role of the stimulation pattern $I^{[d]}$ (and eventually $I^{[m]}$) is of great computational significance.

Using conventional EIT modelling methods, measured data y is essentially the result of the application of a measurement operator M (Green's operator) to electrode potentials U from Equation (4) as

$$y \;=\; MU \tag{5}$$

The steps above essentially reflect the so-called forward EIT problem and are summarised by the non-linear operator $\Lambda : L_2(\Omega) \to \Im^m$,

$$\Lambda(\sigma) \;=\; y \tag{6}$$

which links the interior material distribution $\sigma := \sigma(\mathbf{x}) \in L_2(\Omega)$, $\mathbf{x} \in \Omega$ with the observed data $y \in \Im^m$, where m is the number of measurements. Of interest for EIT imaging is the inverse problem, set out in the next section.

2.2. The inverse problem

The inverse EIT problem is formed as the problem of estimating the unobserved distribution σ from an observable one y. From an optimisation point of view, this can be formed as a quadratic minimisation functional of the form

$$\min_{\sigma} \frac{1}{2}\|\Lambda(\sigma) - y\|_2^2 \tag{7}$$

2.3. The linearised EIT problem

Given a neighbourhood σ_0, the forward operator is said to be Frèchet differentiable, hence application of Taylor's expansion yields the linearised version of the EIT functional as

$$\underbrace{\Lambda^{(1)}(\sigma_0)}_{J}\underbrace{(\sigma - \sigma_0)}_{\delta\sigma} = \underbrace{(\Lambda(\sigma) - \Lambda(\sigma_0))}_{\delta y} + \underbrace{O(\sigma^2)}_{\approx 0} \tag{8}$$

or approximately as

$$J\delta\sigma = \delta y \tag{9}$$

where $\Lambda^{(1)}(\sigma_0)$ is essentially the first order Frèchet differentiation of the non-linear operator Λ at σ_0. Clearly, the dimensionality of J is determined by the dimensionality of the unobservable distribution σ and the measured data y.

2.4. Measured data

In a typical EIT fashion, the measured data vector is contaminated with some noise originating from various physiological, modelling and discretisation errors. Without loss of generality, herein, noise ϵ is assumed as additive. As such,

$$J\delta\sigma = \delta y + \epsilon \tag{10}$$

In a discrete setting, where only a finite set of measurements (y) could be collected, the number of the corresponding discretised equations of Equation (10) is finite. On the other hand, since the number of discretisation variables for σ typically outnumber the dimensionality of the measurements, one encounters a heavily underdetermined problem. From a least squares point of view, the (maximum likehood) analytical solution of the above system results in the solution of the normal set of equations as

$$\delta\sigma = (J^T J)^{-1} J^T (\delta y + \epsilon) \tag{11}$$

Unfortunately, the above solution is of little practical numerical use as the discrete equivalent of J, i.e., $\mathbf{J}$, is a dense, rectangular and ill-conditioned matrix, hence sensitive to numerical errors. Using simple algebra, it is not hard to demonstrate that since $\mathbf{J}$ is anticipated to be ill-conditioned, $(\mathbf{J}^T\mathbf{J})$ is severely ill-conditioned. Hence, one would eventually need to account for this numerical deficiency by means of a regularisation functional R in order to compute a physically meaningful solution. The minimisation functional is now casted as

$$\min_{\sigma} \frac{1}{2}\|J\delta\sigma - \delta y\|_2^2 + R(\sigma) \tag{12}$$

In the Tikhonov regime, typical regularisation candidates are constraints for a bounded solution $R(\sigma) := \frac{1}{2}\lambda\|\sigma\|_2^2$ or, more precisely, for a bespoke penalisation of non-smooth solutions as $R(\sigma) := \frac{1}{2}\lambda\|D\sigma\|_2^2$, where λ is a regularisation parameter, D is a differential operator. The selection of the optimal regularisation parameter and matrix is beyond the scope of this article and is omitted. The reader is kindly referred to [29] for the determination of the λ using, e.g., the L-curve method.

Assuming a Tikhonov based regularisation functional, one now arrives at the (maximum a posteriori) analytical solution

$$\delta\sigma = (J^T J + \lambda D^T D)^{-1} J^T(\delta y + \epsilon) \tag{13}$$

A discussion on non-linear reconstruction methods is omitted. Rather, we refer to [30] and references therein for extensive reviews and discussions.

2.5. SVD & GSVD

In the sequel, the δ-term in the discrete equivalents of $\delta\sigma$, δy, is dropped for notational convenience. Also, real admittivies are now assumed, i.e., conductivities.

The SVD is now employed to facilitate discussion on the interaction between original information contents encapsulated in $\mathbf{J}$ and the artificially imposed prior information matrix $\mathbf{R}$. SVD analysis involves expansion of the linearised system to an orthogonal basis as in the standard Fourier analysis.

The SVD of the (linearised) discrete forward operator $\mathbf{J} \in \Re^{m \times N}$, $m \geq N$, is effectively a decomposition of the form [31]

$$\mathbf{J} = \boldsymbol{P}\boldsymbol{\Xi}\boldsymbol{Q}^T = \sum_{i=1}^{N} \boldsymbol{p}_i \xi_i \boldsymbol{q}_i^T \tag{14}$$

where $\boldsymbol{P} = (\boldsymbol{p}_1, \boldsymbol{p}_2, \ldots, \boldsymbol{p}_m)$ and $\boldsymbol{Q} = (\boldsymbol{q}_1, \boldsymbol{q}_2, \ldots, \boldsymbol{q}_N)$ are matrices with orthonormal columns, i.e., $\boldsymbol{P}^T\boldsymbol{P} = \boldsymbol{Q}^T\boldsymbol{Q} = \mathbf{I}$, called the left and right singular vectors, respectively. The non-negative entries of the diagonal matrix $\boldsymbol{\Xi}$ are typically sorted in non-increasing order as

$$\xi_1 \geq \xi_2 \geq \ldots \xi_N \geq 0 \tag{15}$$

and are identified as the 'singular' values.

In broad terms, the sequential order of the singular values is inversely proportional to information fidelity. Coarse information, associated with low frequencies, is anticipated towards the first singular values, whilst fine detail, encapsulated in high frequencies, is usually concentrated towards the last singular values, i.e., as $i \to N$.

Using SVD, one may determine a generalised inverse $\mathbf{J}^\dagger$ for $\mathbf{J}$, corresponding to the different properties that $\mathbf{J}$ may satisfy. In effect, one may obtain $\mathbf{J}^\dagger$ as

$$\mathbf{J}^\dagger = \sum_{i=1}^{n_\dagger} \boldsymbol{q}_i \xi_i^{-1} \boldsymbol{p}_i^T \tag{16}$$

where

$$n_\dagger := \begin{cases} N, & \text{if } \mathbf{J} \text{ is invertible;} \\ n_r = rank(\mathbf{J}), & \text{if } \mathbf{J} \text{ is } r-\text{rank-deficient.} \end{cases} \tag{17}$$

The first case assumes that $\mathbf{J}$ is of full rank and effectively corresponds to the so called generalised Moore-Penroose 'pseudo inverse' [31]. The second case, which reflects the EIT problem, $\mathbf{J}$ is assumed to be r-rank deficient which implies that some of the smallest singular values are practically zero, i.e.,

$$\xi_1 \geq \ldots \xi_{n_r} \geq \xi_{n_{r+1}} \approx \ldots \approx \xi_N \approx 0 \tag{18}$$

Based on SVD, the Moore-Penrose inverse $\mathbf{J}^\dagger$ can be written in the following form [29]

$$\boldsymbol{\sigma}_\dagger = \mathbf{J}^\dagger \mathbf{y} = \sum_{i=1}^{n_\dagger} \frac{\boldsymbol{p}_i^T \mathbf{y}}{\xi_i} \boldsymbol{q}_i \tag{19}$$

From the above equation, one may study the contribution of the singular values ξ_i and the solution $\boldsymbol{\sigma}_\dagger$ and in fact, understand why SVD provides an insight into the ill-posedness. Generally speaking, should one attempt to invert small singular values $\xi_i \approx 0$, the solution $\boldsymbol{\sigma}_\dagger$ would attract considerably high values, effectively obscuring the desired solution. In this respect, even a small perturbation in $\mathbf{y}$ can cause a dramatically high perturbation in $\boldsymbol{\sigma}_\dagger$ as the tiny values of ξ_i would eventually prevail, rendering the obtained solution meaningless.

An indication of the severity of ill-conditioning is given by the ratio of the largest to the smallest singular value $\kappa_{\mathbf{J}} = \xi_1/\xi_N$ which is also identified as the condition number. The larger the condition number of $\mathbf{J}$, the more severe the ill-posedness of the problem and the more the ill-conditioning it is. The concept of GSVD is now considered, where the main difference between GSVD and SVD is that, rather, a matrix pair is now analysed. In this light,

GSVD provides valuable insight of a matrix coupling. For our needs, the coupling of $\mathbf{R}$, i.e., the selected regularisation matrix, and $\mathbf{J}$ is assumed. In the GSVD setting, the decomposition takes place in a slightly different form for the individual matrices as

$$\mathbf{J} = \boldsymbol{P}\boldsymbol{\Xi}\boldsymbol{X}^{-1}, \quad \mathbf{R} = \boldsymbol{Q}\boldsymbol{M}\boldsymbol{X}^{-1} \tag{20}$$

where matrix $\boldsymbol{X}$ is non-singular and $\boldsymbol{P}$, $\boldsymbol{Q}$ are orthonormal and different from their SVD counterparts. This notational abuse is solely for convenience purposes. In a similar fashion to SVD, matrices $\boldsymbol{\Xi}$ and $\boldsymbol{M}$ are diagonal with normalised entries ξ_i, μ_i, $i = 1, \ldots, p$, $\xi_i^2 + \mu_i^2 = 1$ and for historical reasons arranged in non-decreasing and non-increasing order $0 \leq \xi_i \leq 1$, $1 \leq \mu_i \leq 0$, respectively. The generalised singular values are then

$$\gamma_i = \frac{\xi_i}{\mu_i} \tag{21}$$

In a similar fashion to SVD, one could study the generalised singular values to assess ill-conditioning, however, by taking into account prior information.

3. Picard's stability condition

In [29], the author popularised Picard's criterion as an invaluable insight into the stability of the regularisation problem. In effect, in Picard's criterion the stability of the regularised problem is oriented around the (decay of) Fourier coefficients $|\mathbf{p}_i^T\mathbf{y}|$, or more realistically $|\mathbf{p}_i^T(\mathbf{y} + \boldsymbol{\epsilon})|$ [29]. These coefficients are frequently encountered in the literature as Picard's coefficients. Herein, we adopt this term.

As thoroughly discussed in [29], the key feature exploited in this section is that our measurements are contaminated with noise. It turns out that such errors typically tend to have components along all the left singular vectors $\mathbf{p}_i$. Hence, Picard's coefficients $|\mathbf{p}_i^T(\mathbf{y}+\boldsymbol{\epsilon})|$ of observed data, typically level off around the noise measurement levels. Therefore, in order to maintain stability, one requires that Picard's coefficients decay to zero faster than the generalised singular values γ_i.

This is a great computational quality 'measure', that couples observed data with a priory information (incorporated in the regularisation matrix), without requiring to execute the reconstruction algorithm, e.g., Equation (13). In this regard, it is an *a priory criterion* to comment on the quality, if not effectiveness, of the proposed EIT configuration. Nevertheless, Picard's criterion is a computationally intense, especially for large scale systems as it involves GSVD. On the positive side, one would only need to run this test once and in advance of the reconstruction algorithms, in order to test the suitability of the chosen regularisation matrix for the problem at hand.

In the next section, we scrutinise stimulation patterns under Picard's stability criterion.

4. Putting everything together: Stimulation, measurements & numerical stability

In order to provide a fair comparison between conventional and proposed stimulation, we kick off our numerical simulation with a simple study: We consider a cylindrical tank of uniform background distribution and a spherical perturbation $(x_1+.2)^2+(x_2+.3)^2+(x_3+.4)^2-.1^2<0$ of $\delta\sigma=10\%$

of the background value. One could consider adjacent simulations, however according to [18] little information is acquired with adjacent stimulation patterns so we focus on a standard opposite 2-electrode pair stimulation pattern. For clarity, we opt for a linearised problem, the solution of which is given by Equation (13). Unless otherwise specified, the identity matrix is employed as the regularisation prior, $\mathbf{R}^T\mathbf{R} = \mathbf{I}$. At this stage, the selection of the regularisation matrix is of secondary importance when compared to the selection stimulation pattern. Next, we vary the number of electrode ring number as well as the number of electrodes per ring. In all simulation results, 25dB Gaussian noise ϵ is added to the simulated measurements.

4.1. Simple cylindrical phantom, 2-electrode pair

When $L := 6$ electrodes are available and current is applied to a 2-electrode pair of opposite electrodes, i.e., $I_1 = [1, 0, 0, -1, 0, 0]^T$, one could collect measurements between electrodes $\{2, 3\}$ and $\{5, 6\}$, i.e., $(L-4)$ measurements for this particular current pattern. By shifting the current pattern by one electrode, one arrives at $I_2 = [0, 1, 0, 0, -1, 0]^T$. Repeating for L-electrodes, eventually, one could potentially collect $m := (L-4)L = 12$ measurements, half of which are linearly dependent. Thus, one practically collects a total of $m := L(L-4)/2 = 6$ measurements for $\mathbf{y}$.

Assuming a piecewise constant (per element) approximation in (3), (4), for the real admittivity distribution,

$$\sigma \approx \sum_{i}^{N} \sigma_i \chi_{i=1} \tag{22}$$

where χ_i is the characteristic function and N is the number of elements, the size of the typically underdetermined version of the Jacobian is $\mathbf{J} \in \Re^{m \times N}$,

where practically $m \ll N$. The sensible step therefore is to establish means of increasing the number of measurements m until, ideally, $m \approx N$. This, in turn, entails a significant increase in the number of measurements and, eventually, electrodes L.

Aside from impractical, an increased number of measurements m will contribute towards unrealistically high computational overheads both for the assembly and inversion of the dense matrix $\mathbf{J}$ (not to mention ill-conditioning). Therefore, should a classical 2-pair stimulation and measurement strategy be deployed, a practical upper bound in terms of available computational resources is encountered.

On the other hand, taking into account that we are dealing with an inverse problem, it is essential for stability to only utilise a subset of the available singular values spectrum, as suggested by the singular value analysis of Section 2.5. Moreover, in order to factor in the role of the regularisation matrix $\mathbf{R}$ as well as the presence of the noise in the measurements, the GSVD analysis, in particular, is recalled.

In Figure 1a), a plot of Picard's coefficients along with the generalised singular values γ_i is illustrated for 3 rings of electrodes. Recalling Picard's criterion of Section 3, one requires a faster decay of Picard's coefficients $|\mathbf{p}_i^T(y+\epsilon)|$ than the decay of the generalised singular values γ_i. In [23], the ratio of the generalised singular values that meet Picard's criterion over the total number of available generalised singular values is termed as *gain* of the selected stimulation pattern. Clearly, as it can be depicted from Figure 1a), the majority of singular values is below Picard's threshold. This becomes profound as the number of electrodes increases in the same Figure for the

cases of b) 24, c) 36 and d) 48 electrodes, where notably only a few singular values γ_i survive filtration. The actual gain recorded for each case, when 3 ring of electrodes are considered, is tabulated in Table 1 and termed as **Gain 1**. In the same Table, the ratio of the number of electrodes over the number of measurements is also tabulated to demonstrate how improportional the increase of electrodes is with respect to measurements could be.

In order to further demonstrate that, practically, the quality of gathered measurements is no better when additional electrode rings are added, we repeat the previous experiment. In the new configuration, the number of electrodes remains fixed for each case as before, however, an additional ring of electrodes is allowed. As such, a different electrode distribution is enabled as illustrated in Figure 2. The corresponding gains for the 4-ring systems are now tabulated in Table 2 and termed as **Gain 2**. By coupling Figure 2 and Table 2, it is evident that, assuming fixed number of electrodes for each case, essentially the additional ring allowance, offers very little improvements, if any at all.

Taking into account that the meshing algorithm [32], produces slightly more mesh elements to accommodate the need for the additional ring, gains obtained from **Gain 2** are slightly worse than the ones obtained in **Gain 1** or, in broad terms, in the same range as in **Gain 1**. It is not hard to obtain from Tables 1 & 2 that the additional ring of electrodes results in the same number of measurements and does not yield an overall system improvement in the sense discussed herein.

In fact, one should focus on the fact that, for the given opposite 2-electrode pair stimulation pattern, as the total number of electrodes increases,

both **Gain 1** & **Gain 2** plummet, as more regularisation would indeed be required for stability. In this regard, less singular values would escape filtration. This should be approached as a numerical acknowledgement of the fact that increasing the number of electrodes does not (necessarily) increase the potential information content. Note that this acknowledgement triggers again the earlier question on whether we take the most out of an EIT system, which essentially paves the way for non-conventional stimulation/collection protocols.

4.2. Simple cylindrical phantom - multiple electrode pair

Rather than engaging two electrodes to stimulate currents, we employ a multiple-electrode stimulation pair. That is, opposite *groups of electrodes* are now considered. In order to briefly report on the rationale behind this step, assume that $L = 12$ electrodes are available at our disposal and that the number of desired stimulation patterns is $d = 6$. We now suitably group some of the available electrodes, say 1 group of 2 electrodes, where current is injected, and 1 group of 2 electrodes where current exits the medium. In this way, we are left with $L - 2 \cdot 2 - 2 = 6$ non-current carrying electrodes to gather measurement data. For 6 desired patterns this accounts for $6 \cdot 6 = 36$ measurements. This figure is significantly less than the 96 measurements that would have otherwise needed. The advantage of this stimulation pattern is that although $L = 12$ electrodes were originally considered, the EIT system is essentially clocked with just 36 measurements. In other words, 36 measurements translate to just 37.5% of the overall time required to collect data with the conventional 2-pair opposite protocol.

Given the GSVD discussion of the previous sections, it remains to demon-

strate that the resulting gain for the multiple-electrode pair is better than the conventional one. Intuitively, since more electrodes are involved in the firing process whilst occupying a greater boundary surface, it is sensible to anticipate some gain improvements over the conventional 2-electrode pair stimulation scheme. In other words, one would expect to observe a faster decay in Picard's coefficients than the generalised singular values of the matrix pair $(\mathbf{J}, \mathbf{I})$ for this particular case.

Figure 3 reveals the generalised singular spectrum against Picard's coefficients. The superiority of the proposed scheme materialises from the readings of Table 3, in particular when a large number of electrodes L is considered (**Gain 3**). The naive interpretation of Table 3 is that for the same domain, with the same forward problem parameters and the same regularisation matrix, one could essentially derive an improved system. As in the derived EIT system m is significantly smaller that the original one, so is the linearised problem. Hence, by definition, this is a lower dimension problem so intuitively should be a much faster problem to solve.

The advantages of the proposed scheme become more apparent as more electrodes are engaged in the stimulation process. For clarity, the number of electrode rings is increased to 4 and the corresponding singular spectrum for the 4-ring electrode case is illustrated in Figure 4. As anticipated, a significant gain improvement when compared with **Gain 2** is recorded and the results are tabulated in Table 4 (**Gain 4**).

In the next section, the multiple-electrode pair scheme is applied to a breast phantom.

5. Breast screening with EIT

It is evident from the previous sections that an increased number of electrodes is not necessarily a computational bottleneck. We refrain from discussing methods of accurately extracting the boundary shape of the breast or the technicalities of applying a large number of electrodes to the female breast skin as these topics are beyond the scope of this contribution. Rather, we refer to [21] for accurately extracting boundary surfaces.

Having demonstrated the effectiveness of the proposed scheme, the next sensible task is to report on the performance on a non-identity prior. For this purpose we employ the so called NOSER prior, which is essentially the diagonal of $\mathbf{J}^T\mathbf{J}$. We fix the number of electrodes to $L = 36$ and we illustrate a relatively fine (near the electrodes) mesh of a breast phantom in Figure 6 (top).

The performance of the original stimulation pattern ($L/d = 1$) is illustrated in Figure 5a) and the corresponding gains are tabulated in Table 5. As anticipated, the recorded gain (0.15364) is not far from the one recorded in **Gain 1**, $L = 36$, for the identity prior, i.e., 0.13281, **Gain 5**. However, an increase in the gain measure is reported when, as expected, the more efficient NOSER prior is used (**Gain 6**) for the same case ($L/d = 1$). Next, we test the proposed configuration for $L/d = 2$ electrodes per group against the conventional ($L/d = 1$) one. This action essentially supports the theme of this paper which is swap the single electrode groups for more electrode per group.

In Table 5 one may appreciate the performance of the suggested scheme for the priors considered herein. Clearly, increasing the number of electrodes

per firing-group results in a more efficient systems. This could be further enhanced by the selection of the NOSER prior.

In summary, by suitably 'clocking' an EIT system with an appropriate stimulation pattern as well as an appropriate prior, the performance of the same system could be drastically improved from 0.15364 (**Gain 5**) to 0.9773 (**Gain 6**), not to mention data acquisition and computational times. If more electrodes are considered, say $L = 48$, rather than 2112 measurements, only 180 measurements need to be collected. This accounts for approximately 8.52% of the original measurement number or a saving in the data acquisition time of approximately 91.48%. Thus, for this example, one could not only derive a faster system but could also getaway with a fraction of the conventional measurements.

In order to demonstrate that essentially no compromise in quality of the reconstructed images is reported, we provide some representative reconstruction results. The question of the optimum regularisation value is essentially an active research area where various methods could be used [29]. This is beyond the scope of this paper as the answer lies with the problem at hand and the specifications to be met. Therefore, images are reconstructed for various equidistant logarithmic values for λ, ranging from 1e-1 to 1e-8, i.e., λ ={1.00000e-001, 1.33352e-002, 1.77828e-003, 2.37137e-004, 3.16228e-005, 4.21697e-006, 5.62341e-007, 7.49894e-008, 1.00000e-008}.

For clarity, we present linear reconstructions for the various configurations reflecting the number of electrodes per firing-group, i.e., the conventional one L/d = 1-electrode per group in Figure 7, the proposed one for L/d = 2-electrode per group in Figure 8 and for L/d = 6-electrode per group in

Figure 9. In each Figure, one depicts from the first column 2D coronal slices extracted from the original 3D simulated perturbation. Essentially, we extract 2D reconstructions at levels $\mathbf{h} = [-0.8, -0.6, -0.4, -0.2]^T$, hence 4 images per column. The columns next to the original 3D perturbation, i.e., columns 2-10 in each Figure, are reconstructions for the various values of λ.

To avoid biased reconstructions and essentially an inverse crime, measurements and reconstructions were computed on different meshes. In effect, measurements were collected from the fine mesh for a 10% perturbation, presented in Figure 6 (middle). As mentioned before, 25dB noise was added to the measurements. All reconstructions were performed on a coarser mesh, shown in Figure 6 (bottom). Herein, for all simulations the EIDORS toolbox was employed [26].

6. Discussion

In our view, since EIT is an inverse problem, one should couple proposed stimulation and measurement strategies with prior information. Further, as it is clearly demonstrated by our numerical results, the 1-electrode group, simply put, performs poorly. The advantages of the compound-electrode pair outperform the conventional stimulation methods.

It would be of great interest to verify our numerical findings with realistic measurements. The current bottleneck however, is that most available EIT systems are configured (hardware-wise) to fire on single-electrode groups and are typically manufactured with a little number of electrodes. As such, as long as a multiple-electrode pair system becomes available to our disposal we will publish our findings. Although that we have no mathematical means

to support such a statement at this stage, it appears that a 'more random' choice of non-opposite groups would probably increase the incoherence of $\mathbf{J}$ and would probably improve reconstruction quality.

On the other hand, by using the GSVD analysis, one could essentially provide a good indication of the amount of information that a specific coupling $(\mathbf{J}, \mathbf{R})$ could offer to the inverse problem, before actually solving Equation (13). In this light, it is of little suprise that the identity prior offered very little improvement in the performance of the system. Indeed, the poor performance indicated that major amendments in the selection of the regularisation matrix were necessitated.

6.1. Further work

This study is part of our long term goal to derive model reduction schemes in EIT without compromising on robustness and/or quality of acquired EIT data/images. In this regard, a reduction in m was achieved and essentially reflected in $\mathbf{J}$.

In [15], the author proposed multi-level basis functions (wavelets) as basis functions for both the forward and inverse computations of the soft-field imaging problem in order to reduce dimensionality of $\mathbf{J}$ (by compression). This automatically enabled the 'multi-level Jacobian' and hence the multi-level version of the forward version at no additional computational cost. To the best of our knowledge such a configuration was not available before. It is sensible therefore, to join the ideas developed in this article with the ideas developed in [15] in order to offer a 'possibly primitive' model reduction scheme that makes use of no additional transformation aside from the ones required for the solution of the inverse problem. Needless to say that if ap-

propriate, this could be further combined with other generic model reduction methods, e.g., statistical ones [33], to offer additional significant advantages in reconstruction timings.

On the other hand, there is no restriction on the use of non-linear schemes to perform the reconstruction task. In fact, the proposed method, appears to best suit non-linear systems where linearised steps are essential. Thus, the proposed method has the potential to enable additional computational savings. Not to mention that although real admitivities were considered herein, there is no obvious limitation for the complex case. In this manner, higher frequency model or multi-frequency EIT system could also be studied.

7. Conclusion

In this article, we numerically demonstrated that by engaging more than one electrodes in the stimulation pattern, significant computational savings could be reported. Moreover, it was shown that unlike conventional systems, in the proposed configuration, as the number of electrodes increases so does the performance of the proposed system. Simulations on simple tanks with various numbers of electrode rings and number of electrodes per ring were presented. Ideas developed were then applied to a breast phantom. Representative reconstructions for the breast phantom were provided to emphasise that despite the reduction in the number of collected measurements, no compromise in the quality of the reconstructed images is reported.

Acknowledgements

This work was supported by the Engineering and Physical Sciences Research Council (EPSRC) under Grant EP/G061580/1.

References

[1] WHO, World Health Organisation, http://www.who.int/mediacentre/factsheets/fs297/en/ N297.

[2] BCCUK, Breast cancer care UK, http://www.breastcancercare.org.uk/news/media-centre/facts-statistics.

[3] C. W. Piccoli, Contrast-enhanced breast mri: factors affecting sensitivity and specificity., European Radiology 7 Suppl 5 (1997) 281–288.

[4] P. T. Huynh, A. M. Jarolimek, S. Daye, The false-negative mammogram., Radiographics 18 (5) (1998) 1137–1154.

[5] P. H. Kuo, E. Kanal, A. K. Abu-Alfa, S. E. Cowper, Gadolinium-based MR contrast agents and nephrogenic systemic fibrosis1, Radiology 242 (3) (2007) 647–649.

[6] M. S. Bae, W. Han, H. R. Koo, N. Cho, J. M. Chang, A. Yi, I.-A. Park, D.-Y. Noh, W. S. Choi, W. K. Moon, Characteristics of breast cancers detected by ultrasound screening in women with negative mammograms, Cancer Science 102 (10) (2011) 1862–1867.

[7] M. Soleimani, R. H. Bayford, New and emerging tomographic imaging techniques in medical and industrial applications, Philosophical Trans-

actions of the Royal Society A: Mathematical, Physical and Engineering Sciences 367 (1900) (2009) 3017–3019.

[8] Draeger, Pulmovista 500®, http://www.draeger.com/.

[9] M. Lazebnik, D. Popovic, L. McCartney, C. B. Watkins, M. J. Lindstrom, J. Harter, S. Sewall, T. Ogilvie, A. Magliocco, T. M. Breslin, W. Temple, D. Mew, J. H. Booske, M. Okoniewski, S. C. Hagness, A large-scale study of the ultrawideband microwave dielectric properties of normal, benign and malignant breast tissues obtained from cancer surgeries, Physics in Medicine and Biology 52 (20) (2007) 6093.

[10] M. Assenheimer, O. Laver-Moskovitz, D. Malonek, D. Manor, U. Nahaliel, R. Nitzan, A. Saad, The t-scan technology: electrical impedance as a diagnostic tool for breast cancer detection., Physiological Measurement 22 (1) (2001) 1–8.

[11] N. Polydorides, Image reconstruction algorithms for soft-field tomography, Ph.D. thesis, UMIST, UK (2002).

[12] A. Borsic, Regularisation methods for imaging from electrical measurements, Ph.D. thesis, Oxford Brookes University, UK (2002).

[13] M. Soleimani, Image and shape reconstruction in Magnetic induction and Electrical Impedance Tomography, Ph.D. thesis, University of Manchester (2005).

[14] T. Dai, Image reconstruction in EIT using advanced regularization frameworks, Ph.D. thesis, Carleton University, Canada (2008).

[15] P. Kantartzis, Multilevel soft-field tomography, Ph.D. thesis, City University London, UK (2011).

[16] M. Cheney, D. Isaacson, Distinguishability in impedance imaging, Biomedical Engineering, IEEE Transactions on 39 (8) (1992) 852 –860.

[17] W. R. B. Lionheart, J. Kaipio, C. N. McLeod, Generalized optimal current patterns and electrical safety in EIT, Physiological Measurement 22 (1) (2001) 85.

[18] A. Adler, P. O. Gaggero, Y. Maimaitijiang, Adjacent stimulation and measurement patterns considered harmful, Physiological Measurement 32 (7) (2011) 731.

[19] A. Adler, R. Youmaran, W. R. B. Lionheart, A measure of the information content of EIT data, Physiological Measurement 29 (6) (2008) S101.

[20] A. Boyle, A. Adler, The impact of electrode area, contact impedance and boundary shape on EIT images, Physiological Measurement 32 (7) (2011) 745.

[21] J. Forsyth, A. Borsic, R. J. Halter, A. Hartov, K. D. Paulsen, Optical breast shape capture and finite-element mesh generation for Electrical Impedance Tomography, Physiological Measurement 32 (7) (2011) 797.

[22] H. Dehghani, N. Soni, R. Halter, A. Hartov, K. D. Paulsen, Excitation patterns in three-dimensional Electrical Impedance Tomography, Physiological Measurement 26 (2) (2005) S185.

[23] N. Polydorides, H. McCann, Electrode configurations for improved spatial resolution in Electrical Impedance Tomography, Measurement Science and Technology 13 (12) (2002) 1862.

[24] N. Soni, K. Paulsen, H. Dehghani, A. Hartov, Finite element implementation of maxwell's equations for image reconstruction in electrical impedance tomography, Medical Imaging, IEEE Transactions on 25 (1) (2006) 55 –61.

[25] N. Polydorides, W. R. B. Lionheart, A matlab toolkit for three-dimensional electrical impedance tomography: a contribution to the electrical impedance and diffuse optical reconstruction software project, Meas. Sc. Tech. 13 (12) (2002) 1871–1883.

[26] EIDORS, Electrical impedance tomography and diffuse optical tomography reconstruction software, http://eidors3d.sourceforge.net/.

[27] N. Polydorides, W. R. B. Lionheart, Adjoint formulations in impedance imaging, Proc. 3rd Cong. Indust. Proc. Tomog.

[28] E. Somersalo, M. Cheney, D. Isaacson, Existence and uniqueness for electrode models for electric-currentcomputed tomography, SIAM J. App. Math. 52 (4) (1992) 1023–1040.

[29] P. C. Hansen, Rank deficient and discrete ill-posed problems, SIAM, Philadelphia, PA, USA, 1998.

[30] O. Scherzer, Handbook of Mathematical Methods in Imaging, 1st Edition, Springer-Verlag, 2010.

[31] G. H. Golub, C. F. Van Loan, Matrix Computations, 2nd Edition, Johns Hopkins Press, Baltimore, MD, 1989.

[32] J. Schorberl, Netgen - an Advancing front 2d/3d mesh generator based on abstract rules, Computing and Visualization in Science 1 (1) (1997) 41–52.

[33] A. Nissinen, L. M. Heikkinen, J. P. Kaipio, The bayesian approximation error approach for electrical impedance tomographyexperimental results, Measurement Science and Technology 19 (1) (2008) 015501.

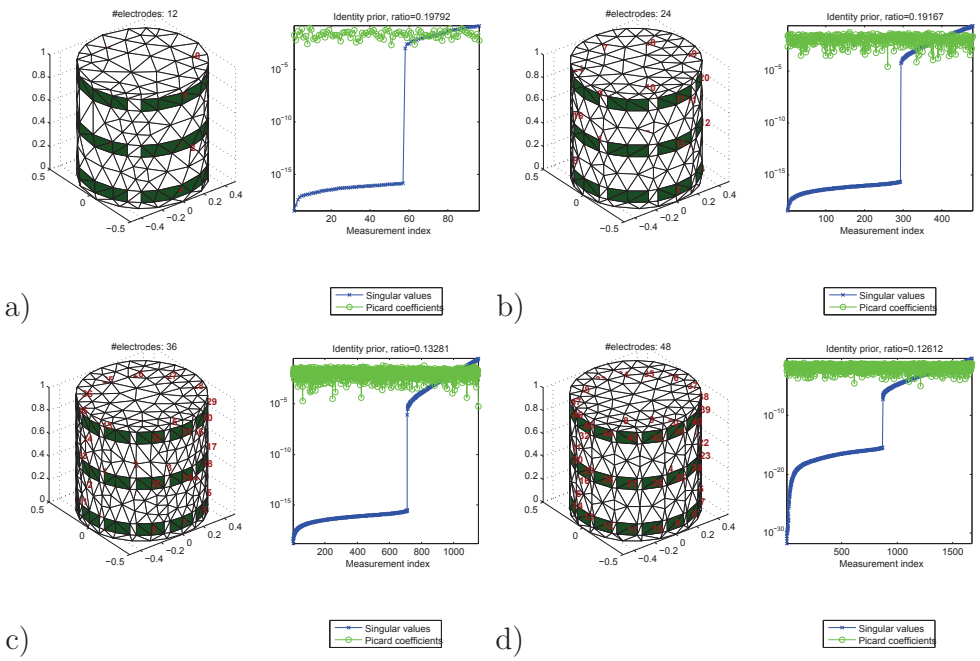

Figure 1: Conventional opposite 2-electrode pair stimulation protocol: Picard's coefficients superimposed to the generalised singular values for a cylindrical tank test phantom where 3 rings of electrodes are attached. The total number of electrodes is a) 12, b) 24, c) 36 and d) 48.

Electrodes L	**Measurements** m	L/m	**Gain 1**
12	96	0.12500	0.19792
24	480	0.05000	0.19167
36	1152	0.03125	0.13281
48	2112	0.02273	0.12612

Table 1: Conventional opposite 2-electrode pair stimulation protocol gains: **Gain** is the ratio of the practically available generalised singular values against the total number of generalised singular values for a cylindrical tank test phantom where 3 rings of electrodes are allowed.

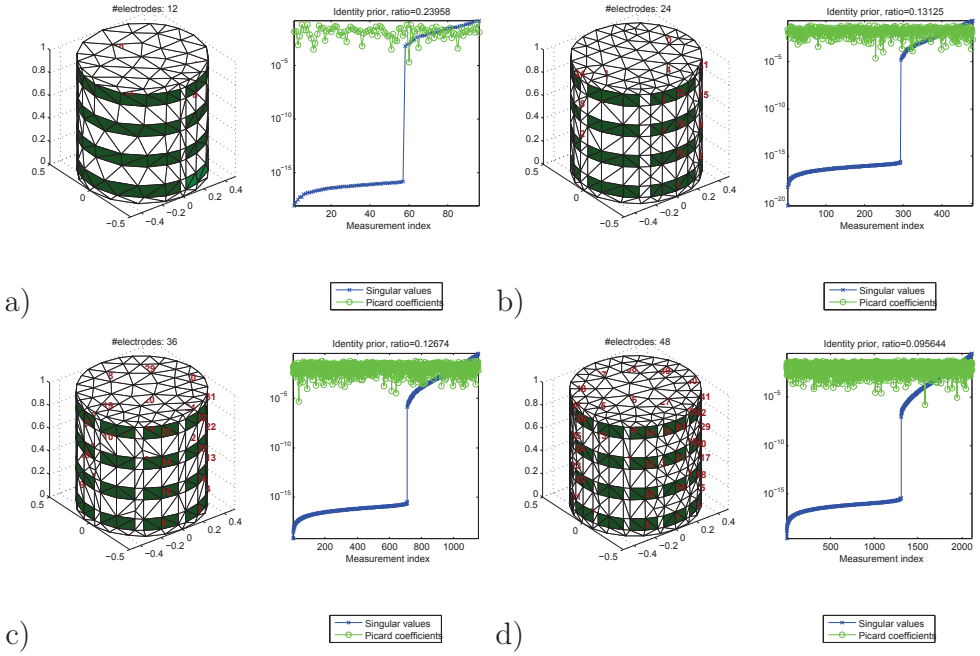

Figure 2: Conventional opposite 2-electrode pair stimulation protocol: Picard's coefficients superimposed to the generalised singular values for a cylindrical tank test phantom where 4 rings of electrodes are attached. The total number of electrodes is a) 12, b) 24, c) 36 and d) 48.

Electrodes L	**Measurements** m	L/m	**Gain 2**
12	96	0.12500	0.23958
24	480	0.05000	0.13125
36	1152	0.03125	0.12674
48	2112	0.02273	0.09564

Table 2: Conventional opposite 2-electrode pair stimulation protocol gains: **Gain** is the ratio of the practically available generalised singular values against the total number of generalised singular values for a cylindrical tank test phantom where 4 rings of electrodes are allowed.

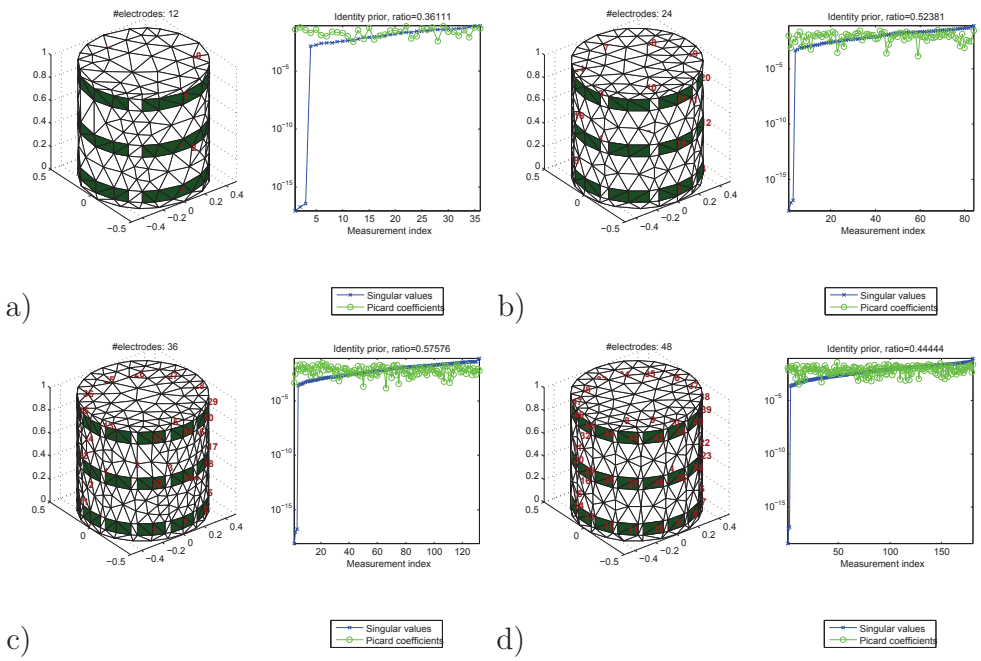

Figure 3: Proposed opposite protocol ($d = 6$ driving patterns): Picard's coefficients superimposed to the generalised singular values for a cylindrical tank test phantom where 3 rings of electrodes are attached. The total number of electrodes is a) 12, b) 24, c) 36 and d) 48.

Electrodes L	**Measurements** m	L/m	**Gain 3**
12	36	0.33333	0.36111
24	84	0.28571	0.52381
36	132	0.27273	0.57576
48	180	0.26667	0.44444

Table 3: Proposed opposite protocol gains ($d = 6$ driving patterns): **Gain** is the ratio of the practically available generalised singular values against the total number of generalised singular values for a cylindrical tank test phantom where 3 rings of electrodes are allowed.

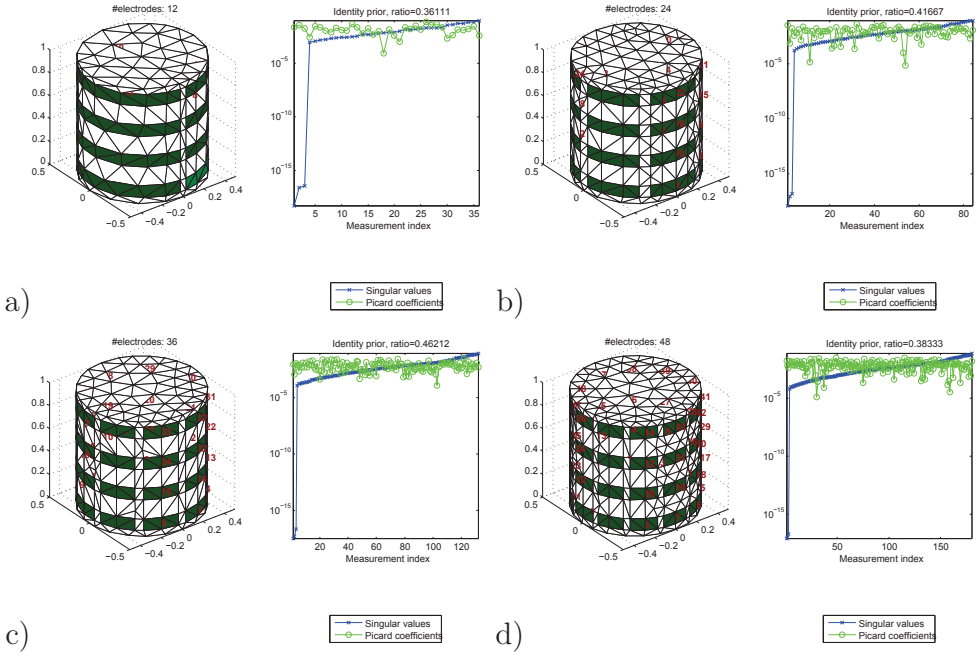

Figure 4: Proposed opposite protocol ($d = 6$ driving patterns): Picard's coefficients superimposed to the generalised singular values for a cylindrical tank test phantom where 4 rings of electrodes are attached. The total number of electrodes is a) 12, b) 24, c) 36 and d) 48.

Electrodes L	**Measurements** m	L/m	**Gain 4**
12	36	0.33333	0.36111
24	84	0.28571	0.41667
36	132	0.27273	0.46212
48	180	0.26667	0.38333

Table 4: Proposed opposite protocol gains ($d = 6$ driving patterns): **Gain** is the ratio of the practically available generalised singular values against the total number of generalised singular values for a cylindrical tank test phantom where 4 rings of electrodes are allowed.

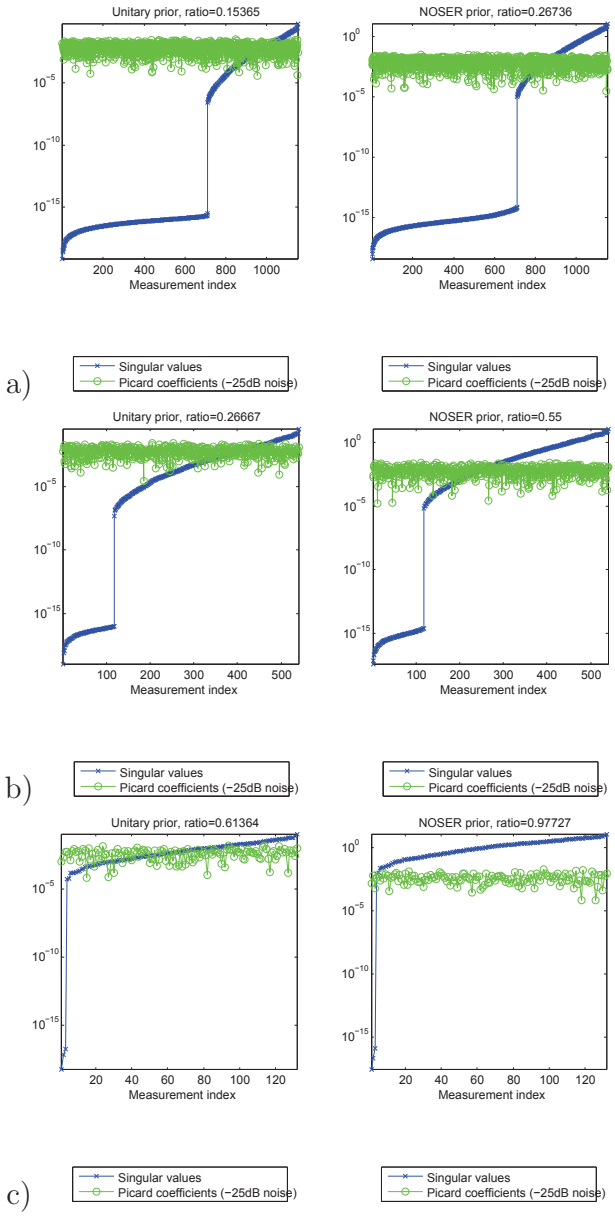

Figure 5: Conventional versus proposed opposite protocol for various numbers L/d of electrodes per stimulation group. a) $L/d = 1$, b) $L/d = 2$ and c) $L/d = 6$ electrodes per groups. In the left column results shown assume a simple identity prior and in the right column results shown assume the NOSER prior.

L/d	**Electrodes** L	**Measurements** m	L/m	**Gain 5**	**Gain 6**
1	36	1152	0.03125	0.15364	0.26736
2	36	540	0.06671	0.26673	0.55001
6	36	132	0.27274	0.61361	0.97731

Table 5: Comparison between conventional ($L/d = 1$) and proposed ($L/d = 2, 6$) opposite protocol gains for the breast phantom. Priors considered herein are the Identity (**Gain 5**) and the NOSER (**Gain 6**) one.

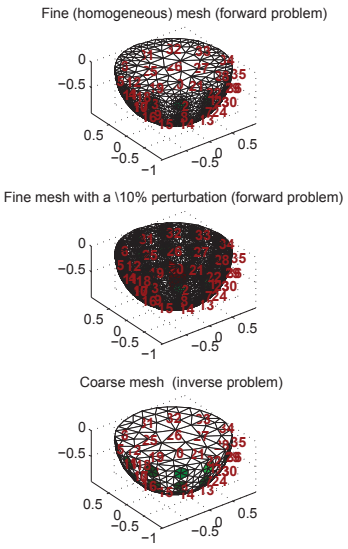

Figure 6: Breast phantom meshes: (Top, middle) Fine meshes used to simulate measurements. In the middle a 10%, 3D perturbation is shown. (bottom) A coarser mesh to be used for reconstruction purposes.

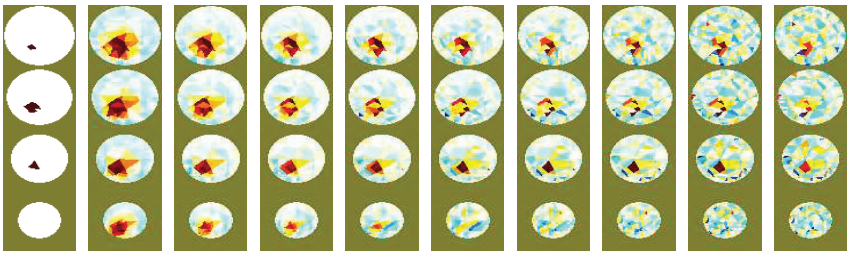

Figure 7: Conventional opposite protocol ($L/d = 1$ electrodes per group). First column is the original 3D perturbation presented as 2D coronal slices of the breast phantom at levels **h**. Remaining columns (2-10) are reconstructions for various values of the regularisation parameter λ={1.00000e-001, 1.33352e-002, 1.77828e-003, 2.37137e-004, 3.16228e-005, 4.21697e-006, 5.62341e-007, 7.49894e-008, 1.00000e-008}.

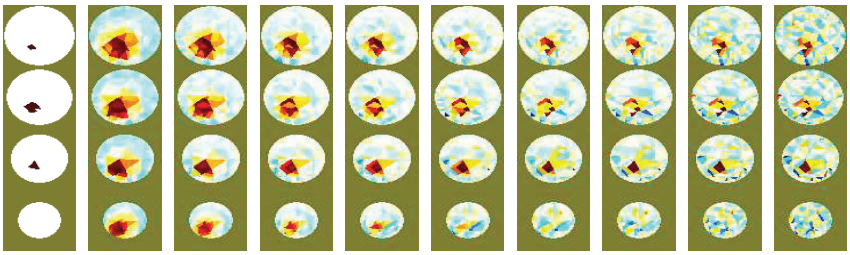

Figure 8: Proposed opposite protocol ($L/d = 2$ electrodes per group). First column is the original 3D perturbation presented as 2D coronal slices of the breast phantom at levels **h**. Remaining columns (2-10) are reconstructions for various values of the regularisation parameter λ={1.00000e-001, 1.33352e-002, 1.77828e-003, 2.37137e-004, 3.16228e-005, 4.21697e-006, 5.62341e-007, 7.49894e-008, 1.00000e-008}.

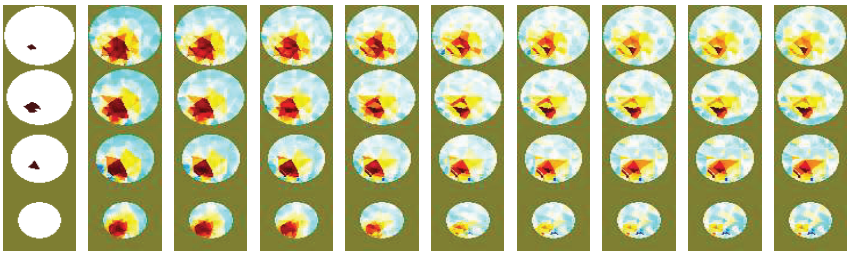

Figure 9: Proposed opposite protocol ($L/d = 6$ electrodes per group). First column is the original 3D perturbation presented as 2D coronal slices of the breast phantom at levels **h**. Remaining columns (2-10) are reconstructions for various values of the regularisation parameter λ={1.00000e-001, 1.33352e-002, 1.77828e-003, 2.37137e-004, 3.16228e-005, 4.21697e-006, 5.62341e-007, 7.49894e-008, 1.00000e-008}.

Highlights:

- Improved stimulation protocol for 3D impedance imaging;
- Suitable for excessive electrodes in 3D geometries, e.g., breast imaging;
- Reduction in number of measurements and data acquisition timings;
- Improved performance for the same impedance imaging system;
- No compromise on the quality of reconstructed images;